Electrical and optical properties of thin films consisting of tin-doped indium oxide nanoparticles

J. Ederth

Department of Engineering Sciences, The Ångström Laboratory, Uppsala University, P.O. Box 534, SE-751 21 Uppsala, Sweden

P. Johnsson

Department of Condensed Matter Physics, Royal Institute of Technology, S-164 40, Stockholm-Kista, Sweden

G. A. Niklasson, A. Hoel, A. Hultåker,* P. Heszler,[†] and C. G. Granqvist

Department of Engineering Sciences, The Ångström Laboratory, Uppsala University, P.O. Box 534, SE-751 21 Uppsala, Sweden

A. R. van Doorn and M. J. Jongerius

Philips CFT, P.O. Box 218/SAQ, 5600 MD Eindhoven, The Netherlands

D. Burgard

Nanogate GmbH, Gewerbepark Eschberger Weg, 661 21 Saarbrücken, Germany

Electrical transport and optical properties were investigated in porous thin films consisting of In_2O_3:Sn (indium tin oxide, ITO) nanoparticles with an initial crystallite size of ~ 16 nm and a narrow size distribution. Temperature dependent resistivity was measured in the $77 < t < 300$ K temperature interval for samples annealed at a temperature in the $573 \leq t_A \leq 1073$ K range. Samples annealed at $573 \leq t_A \leq 923$ K exhibited a semiconducting behavior with a negative temperature coefficient of the resistivity (TCR). These data were successfully fitted to a fluctuation induced tunneling model, indicating that the samples comprised large conducting clusters of nanoparticles separated by insulating barriers. Samples annealed at $t_A = 1073$ K displayed a metallic behavior with no signs of insulating barriers; then the TCR was positive at $t > 130$ K and negative at $t < 130$ K. Effects of annealing on the ITO nanoparticles were investigated by analyzing the spectral optical reflectance and transmittance using effective medium theory and accounting for ionized impurity scattering. Annealing was found to increase both charge carrier concentration and mobility. The ITO nanoparticles were found to have a resistivity as low as 2×10^{-4} Ω cm, which is comparable to the resistivity of dense high quality In_2O_3:Sn films. Particulate samples with a luminous transmittance exceeding 90% and a resistivity of $\sim 10^{-2}$ Ω cm were obtained.

I. INTRODUCTION

Materials exhibiting a high visible transparency and good electrical conductance are interesting for several important applications, and can be used as transparent electrodes for display devices, as well as in solar cells.[1] Transparent conducting oxides attract particular interest, with In_2O_3:Sn (known as indium tin oxide, ITO) being the most widely studied alternative. Many investigations have been performed on electrical and optical properties of ITO produced with different methods, such as physical vapor deposition[2–4] and spray pyrolysis.[5] High quality ITO films have a resistivity as low as $\sim 10^{-4}$ Ω cm in combination with a high visible transmittance.[6] The optical band gap lies between 3.75 and 4.55 eV depending on the amount of Sn doping and the accompanying charge carrier concentration.[7]

ITO films, to be used as front-surface electrodes in display devices, are normally produced by a process involving several steps, such as film deposition followed by etching to obtain the desired patterned structure. Patterning is time consuming and hence costly, and it would be a significant improvement if the etching could be eliminated and replaced by a direct printing process wherein ITO nanoparticles are dispersed in a liquid and applied directly onto the substrate. A subsequent heat treatment of the film would then give a high visible transmittance and a low resistivity. Thus far only a few results have been published concerning electrical transport properties of such nanoparticle/nanocrystalline ITO films.[8–11]

In this paper we report on temperature dependent electrical transport and optical properties of porous thin films consisting of ITO nanoparticles produced by a wet-chemical method. The films were spin coated from a dispersion of ITO nanoparticles with a narrow size distribution. In a practical application, the dispersion would be printed directly onto the substrate to produce fine-patterned structures. However, in this work large area depositions were preferred in order to enable analyses of the optical and electrical properties of the nanoparticle films.

Sections II and III below describe the sample preparation and sample characterization, respectively. Theoretical considerations concerning electrical transport and optical properties are then presented in Sec. IV, and experimental results are given in Sec. V. Specifically we show that the dc electrical transport properties are dominated by thermally activated voltage fluctuations across insulating barriers between large metallic clusters of individual nanoparticles in the sample, giving a negative temperature coefficient of the resistivity.[12]

TABLE I. Sample data showing annealing temperature t_A for treatment at 1 h in air and 1 h in N_2, lattice parameter a, and mean grain size d.

Sample	t_A ($°$C)	a (nm)	d (nm)
A	300	1.0150	16
B	400	1.0144	16
C	500	1.0156	16
D	650	1.0150	19
E	800	1.0147	34

The results from the optical spectroscopy measurements were fitted to the Bruggeman effective medium model,[13] including the effect of ionized impurity scattering, i.e., electrons scattered by dopant Sn^{4+} ions introduced in the material. Fitting theoretical data to experimental results made it possible to determine the charge carrier concentration and mobility in the ITO nanoparticles after annealing to different temperatures. We analyzed annealing-dependent changes of the volume fraction of ITO in the film, related to the density of the samples, and obtained valuable data on the efficiency of the sintering. Finally Secs. VI and VII present a discussion and conclusions of the results in this work.

II. SAMPLE PREPARATION

ITO nanoparticles with a tin to indium atomic ratio of 5% were produced by a commercial wet-chemical method (Nanogate GmbH). The primary particle diameter size was ~ 16nm as measured by a laser back scattering method using a LECOTRAC LTU-150 Ultrafine Particle Size Analyzer. Thin films were produced by spin coating a dispersion of the ITO nanoparticles onto glass substrates. The film thickness, measured by a Dektak 3030 mechanical stylus profilometer, was found to be ~ 1.1 μm.

Rutherford backscattering (RBS) measurements combined with thickness measurements indicated a highly porous structure, i.e., a low density, with a filling factor of ITO nanoparticles in the range 30–40 vol%. Scanning electron microscopy investigations of these samples supported the notion of a highly porous film structure.[14] Post-deposition annealing was carried out in the temperature interval $573 \leqslant t_A \leqslant 1073$ K. The heating rate was 10 K/min. At each temperature, annealing was performed initially for 1 h in air followed by annealing for 1 h in a N_2 atmosphere. Table I presents the samples and their corresponding t_As.

III. SAMPLE CHARACTERIZATION

All samples were characterized using x-ray diffractometry (Siemens D5000 diffractometer) employing CuK_α radiation with a wavelength of 0.15405 nm. Figure 1 presents a diffractogram of sample A. The peaks were consistent with In_2O_3 (Powder Diffraction File 06-0416) and no peaks pertinent to other crystalline structures were observed.

Determinations of lattice parameter a were carried out using Si powder as a reference with a well defined (111)
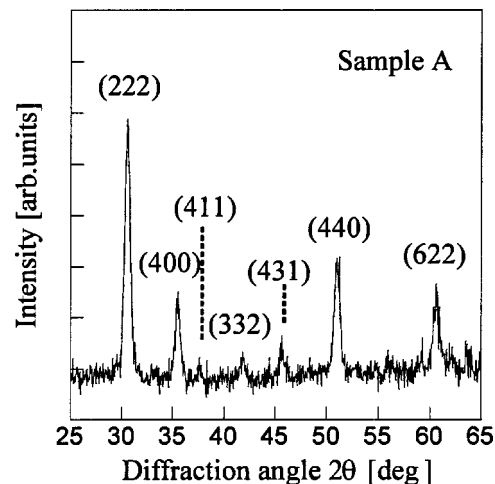

FIG. 1. X-ray diffractogram of ITO (sample A). The peak intensities are labeled according to the major peaks of In_2O_3.

peak, put on top of each sample, and a was obtained from the (222) peak corresponding to In_2O_3. Data on a are given in Table I for all samples. It is found that the lattice parameter remains constant for annealing to 1073 K with a value slightly larger to that of pure In_2O_3, i.e., $a = 1.0118$ nm. The enhancement of the lattice parameter may be due to the tin doping causing a distortion of the In_2O_3 lattice.

Scherrer's method[15] was employed to estimate grain size d. The (222) peak in the diffractogram was used, and data are given in Table I. It is well known that effects of lattice strains may give additional peak broadening, thus resulting in an erroneous grain size. Figure 2 presents scanning electron micrographs of three samples annealed at the shown annealing temperatures, thus providing independent information on the grain size. Data from the two analysis methods were in satisfactory agreement, with the difference in the mean grain size lying below 5%. The grain size was found to be constant up to $t_A = 773$ K. Annealing at 923 K resulted in a grain growth to 19 nm, and the final annealing at 1073 K produced a significant increase of d to 34 nm.

Figure 3 shows ITO nanoparticle size distributions of the five different samples. The distributions were determined by measuring the diameter of more than 200 individual nanoparticles shown on scanning electron micrographs. It is observed that the size distributions are very similar and narrow for samples A–C; see Figs. 3(a)–3(c). Annealing at high temperature gives an increased mean particle size and the size-distribution becomes wider; see Figs. 3(d) and 3(e).

IV. THEORETICAL CONSIDERATIONS

A. Electrical transport

Temperature dependent electrical transport in semiconductor materials is a complex property, whose reconciliation with theory demands a detailed knowledge of the local electronic structure. A theoretical modeling is also made difficult by the fact that there are several different transport mechanisms exhibiting a negative temperature coefficient of the resistivity (TCR); among these one finds tunneling and hopping conduction.
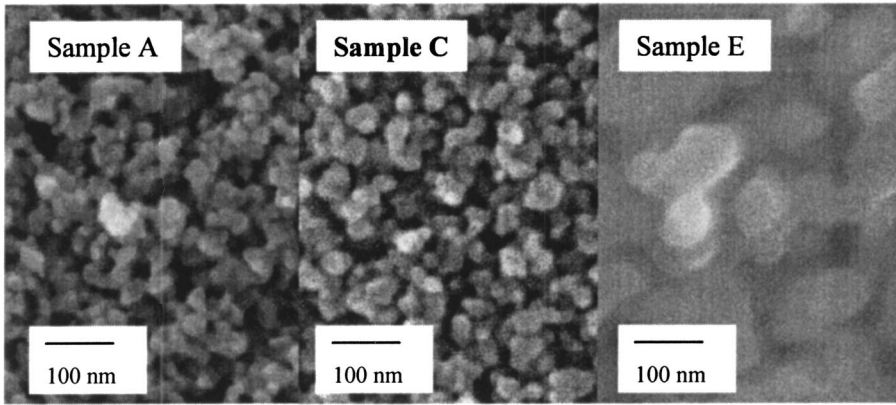
FIG. 2. Scanning electron micrographs for samples A, C, and E characterized in Table I.

Below we consider electrical transport mechanisms yielding a negative TCR, starting with hopping mechanisms and following with a transport mechanism dominated by the capacitive charging energy in a system consisting of a distribution of individually isolated small metal particles. Temperature dependent resistivity in a system consisting of large conducting clusters of individual nanoparticles, separated by thin insulating layers, is also considered. This section ends with the effect of ionized impurity scattering on the temperature dependent resistivity.

Hopping conduction can be represented by an exponential temperature dependent resistivity $\rho(t)$ of the form[16]

$$\rho(t) = B_1 \exp\left[\left(\frac{B_2}{t}\right)^{1/q}\right], \tag{1}$$

where B_1, B_2, and q are constants. A conduction mechanism dominated by hopping between localized states distributed randomly in the film (i.e., variable range hopping, VRH) yields a temperature dependence as described by Eq. (1) with $q=4$.[16] Another hopping conduction mechanism, characterized by $q=1$, is representative of localized states distributed in a periodic array (i.e., nearest neighbor hopping, NNH).[16] The granular-metal system is characterized by a distribution of small metallic grains separated by thin insulating layers. In such systems, the resistivity is governed by a charging energy E_c, which is inversely proportional to a capacitance C, i.e.,

$$E_c = \frac{\eta e^2}{2C}, \tag{2}$$

where η is a constant and e is the electronic charge. A small particle size gives a small capacitance, which results in a large E_c. Then $\rho(t)$ is dominated by electrons hopping between the metal grains. The corresponding granular-metal model (GM) is given by Eq. (1) with $q=2$.[16]

A different temperature dependent resistivity appears if the metallic regions can be regarded as large internally connected clusters separated by thin insulating layers. This yields a much higher total capacitance, which results in E_c being negligible compared to the thermal energy $k_B t$, where k_B is Boltzmann's constant. In such samples the resistivity is dominated by fluctuation induced tunneling between the metallic regions, and $\rho(t)$ is given by[12]

$$\rho(t) = B_3 \exp\left(\frac{t_1}{t+t_0}\right), \tag{3}$$

where B_3 is a constant and t_0 and t_1 are related to the properties of the insulating barriers between the metallic clusters and obtained from[17]

$$t_0 = \frac{16\varepsilon_0 \hbar A V_0^{3/2}}{\pi(2m)^{1/2} w^2 e^2 k_B} \tag{4}$$

and

$$t_1 = \frac{8\varepsilon_0 A V_0^2}{e^2 k_B w}. \tag{5}$$

Here A is the barrier area, V_0 is the barrier height, m is the charge carrier mass, w is the width of the barrier, ε_0 is the permittivity for free space, and $\hbar$ is Planck's constant divided by 2π.

Ionized impurities are an important source of scattering in doped semiconductors. If this scattering dominates, the TCR is negative and the temperature dependent drift mobility is given by[18]

$$\mu(t) \propto t^{3/2}. \tag{6}$$

In a heavily doped degenerate semiconductor, the temperature dependent charge carrier concentration due to intrinsic carriers is negligible because of the high doping level. Thus the temperature dependence of $\rho(T)$ is given by $\mu(T)$, so that

$$\rho(t) \propto t^{-3/2}. \tag{7}$$

B. Optical properties

Low density nanoparticle films can, from a theoretical point of view, not be treated as homogeneous samples. In a recent paper[19] we successfully applied an effective medium theory by Bruggeman (Br) to fit spectral reflectance and transmittance data of porous ITO nanoparticle films. Information on charge carrier concentration n_e, mobility μ, and filling factor f of the ITO nanoparticles—i.e., the volume
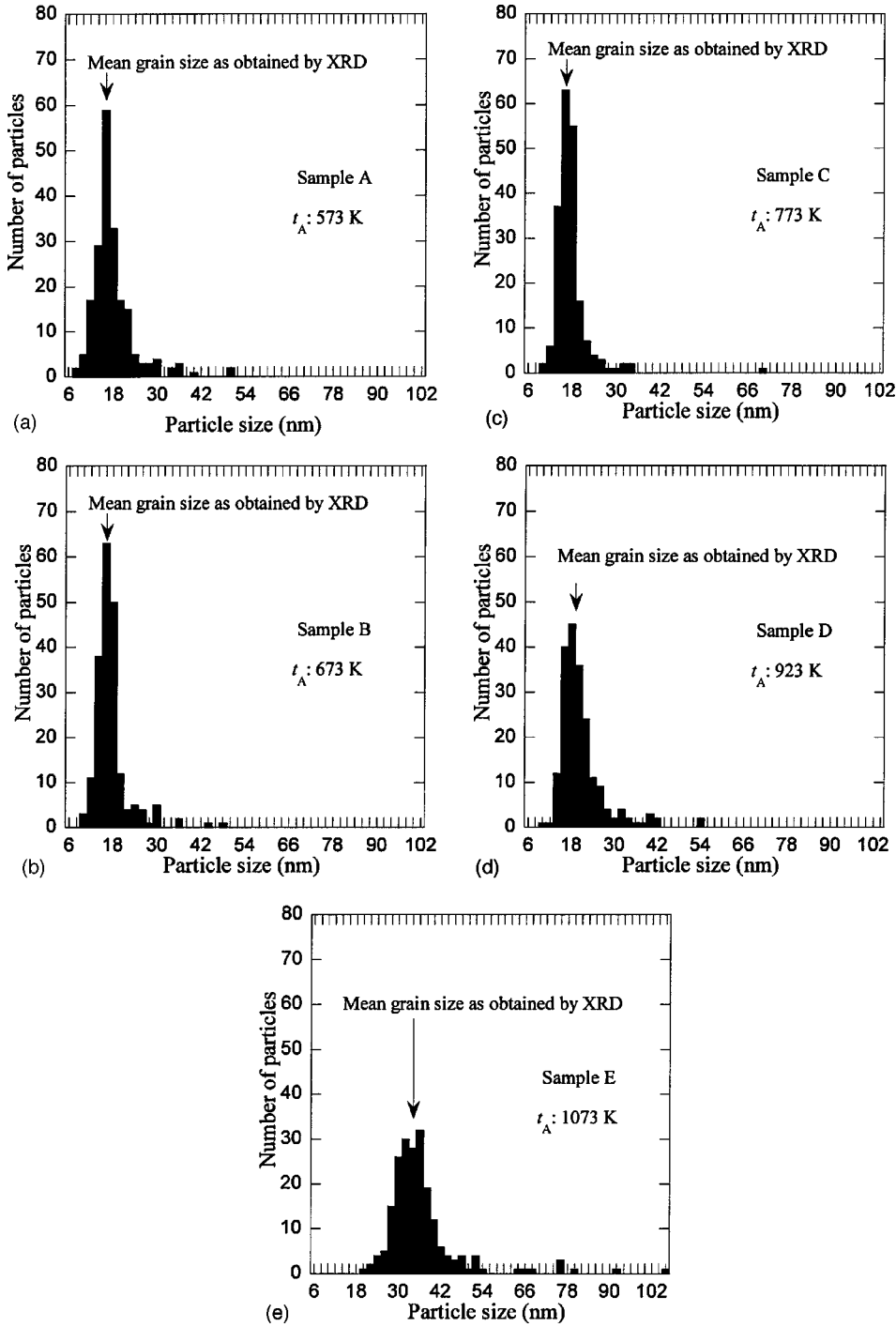
FIG. 3. (a)–(e) Size distributions for the five samples specified in Table I.

fraction of ITO in the sample—were obtained from the fitting parameters. The same approach is used here to analyze changes in these parameters upon annealing. Our samples are modeled as consisting of spherical ITO nanoparticles connected in a percolating network surrounded by air. The Bruggeman model for spherical particles reads[13]

$$f \frac{\varepsilon_p - \bar{\varepsilon}^{\mathrm{Br}}}{\varepsilon_p + 2\bar{\varepsilon}^{\mathrm{Br}}} + (1-f) \frac{\varepsilon_a - \bar{\varepsilon}^{\mathrm{Br}}}{\varepsilon_a + 2\bar{\varepsilon}^{\mathrm{Br}}} = 0, \qquad (8)$$

where ε_p is the dielectric function for the ITO nanoparticles, ε_a is the dielectric function for air, and $\bar{\varepsilon}^{\mathrm{Br}}$ is the effective medium dielectric function.

For heavily doped indium oxide, as in the case of our ITO nanoparticles, n_e easily exceeds the Mott critical density [$\sim 4 \times 10^{18}$ cm^{-3} for ITO (Ref. 20)] so that the Fermi energy level is located above the minimum of the conduction band. This gives free electrons in the conduction band of the ITO nanoparticles, and we may represent their dielectric function by the Drude model. The Drude model is given by

$$\varepsilon_p = \varepsilon_\infty - \frac{\omega_p^2}{\omega \left(\omega + i \dfrac{1}{\tau_0} \right)}, \qquad (9)$$
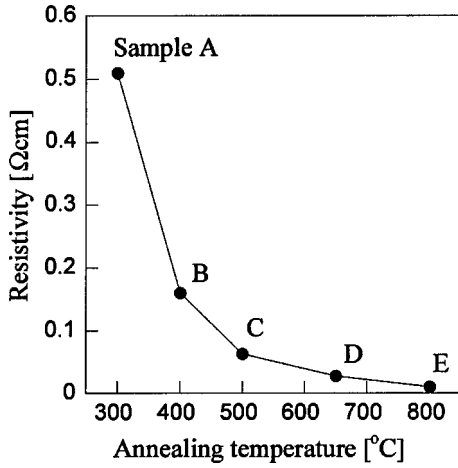
FIG. 4. Room temperature resistivity as a function of annealing temperature for the samples characterized in Table I. Dots indicate data and lines were drawn for convenience.

with ω_p and τ_0 according to

$$\omega_p^2 = \frac{n_e e^2}{m_e \varepsilon_0}, \tag{10}$$

$$\tau_0 = \frac{m_e}{\rho_p n_e e^2}. \tag{11}$$

Here ε_∞ is the optical dielectric constant, ω_p the plasma frequency, τ_0 the relaxation time, m_e the effective electron mass, and ρ_p the resistivity of the ITO nanoparticles.

Earlier work by Hamberg and Granqvist[21] supported the use of Drude theory to model the dielectric function of ITO provided that an energy dependent relaxation time is used in the energy range between the band gap and the screened plasma frequency. In heavily doped ITO, this relaxation time is due to electrons scattered by ionized dopant atoms, i.e., ionized impurity scattering (IIS) prevails. At frequencies higher than the screened plasma frequency we compare data based on a frequency dependent relaxation time due to ionized impurity scattering[21] and a constant effective relaxation time according to Drude theory. At frequencies lower than the screened plasma frequency, a constant relaxation time is used. In the case of ionized impurity scattering, the frequency dependent relaxation time is given by[21]

$$\tau^{\mathrm{IIS}}(\omega) = \tau_0 \left(\frac{\omega_p}{\sqrt{\varepsilon_\infty}} \right)^{-3/2} \omega^{3/2}, \tag{12}$$

where $\omega_p/\sqrt{\varepsilon_\infty}$ is the screened plasma frequency. We put $\varepsilon_\infty = 4$ in the calculations and used $m_e = 0.4\,m$, where m is the free electron mass.[21] The filling factor in the Bruggeman model is related to the sample resistivity in the dc limit as[22]

$$\rho = \rho_p \left(\frac{1 - f_c}{f - f_c} \right), \tag{13}$$

where ρ is the resistivity measured for the film and f_c is the filling factor corresponding to the percolation limit, which is 0.33 in the Bruggeman model. Thus Eq. (13) makes it pos-
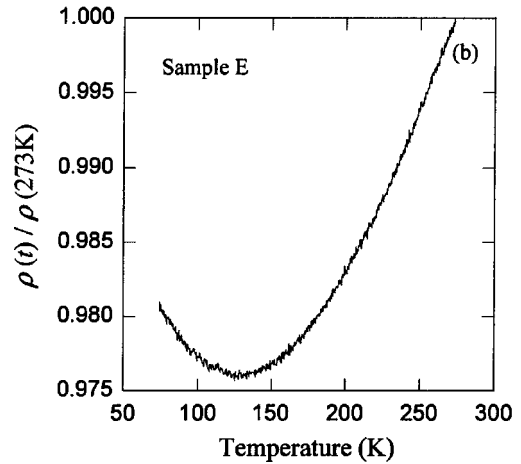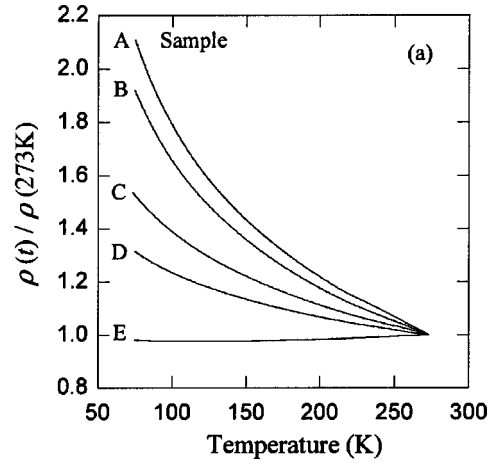

FIG. 5. Normalized resistivity ρ vs temperature t for the samples characterized in Table I. Part (a) represents data for all samples, and part (b) amplifies the resistivity change for sample E.

sible to relate the measured dc resistivity to the resistivity obtained by fitting the Bruggeman model to the experimental data, as considered in Sec. V.

V. RESULTS

A. Electrical data and analysis

Temperature dependent resistivity measurements were performed using a standard four-probe setup. All samples were cut into 7×7 mm^2 squares, and four electrodes were mounted in the corners using silver paste. Resistance was measured by applying a constant current of 500 μA, using a Keithley 2400 source instrument, and measuring the voltage using a Keithley 2002 voltmeter. The heating rate was set to 2.5 K/min.

Figure 4 presents room temperature resistivity data for all samples. It is clearly displayed that the resistivity is decreased upon annealing. Sample E exhibits a resistivity of $\sim 1 \times 10^{-2}$ Ω cm, which is much larger than the minimum value found in the literature, viz. $\sim 1 \times 10^{-4}$ Ω cm.[23,24] However, one should take into consideration that the present samples exhibit a large degree of porosity, as evident from the filling factor being 0.33–0.35.
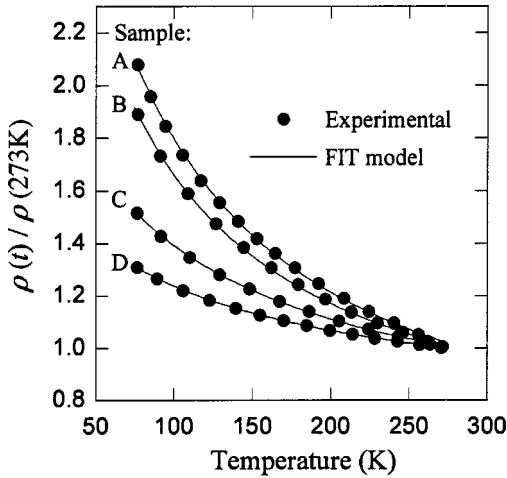
FIG. 6. Normalized resistivity ρ versus temperature t for samples A–D characterized in Table I. Experimental data are shown together with computations from the fluctuation induced tunneling model [Eq. (3)] using the fitting parameters in Table II.

Measurements of temperature dependent resistivity $\rho(t)$ were carried out in the $77 < t < 300$ K range. Figure 5 shows that samples A–D exhibit a negative TCR in the whole temperature range, whereas the temperature dependent resistivity of sample E displays a metallic-like behavior with a positive TCR in the $150 < t < 300$ K range. At approximately 130 K, the resistivity of this sample reaches a minimum and at $t < 130$ K the temperature dependent resistivity has a negative TCR.

There are several different electrical transport mechanisms that can yield a negative TCR, as discussed in Sec. IV above, and next we analyze the $\rho(t)$ data of samples A–D in order to obtain information on which mechanism is dominating in our porous ITO nanoparticle films.

The experimental resistivity data for samples A–D are compared to data obtained from the fluctuation induced tunneling model in Fig. 6. Good agreement is observed for all samples in the whole temperature range. The fitting parameters, i.e., t_0 and t_1, are given in Table II.

Figure 7 presents data for samples A–D plotted as log $\rho(t)$ versus $t^{-1/q}$ with $q=4$, corresponding to the VRH model for electrical transport, as introduced above. A straight-line fit would indicate that this theoretical model applies. Since the curve deviates from a linear fit by a concave curvature, VRH is not valid for the transport mechanism present in these samples. Furthermore we can conclude, from

TABLE II. Data for the fitting parameters t_0 and t_1 in the fluctuation induced tunneling model; see Eq. (2).

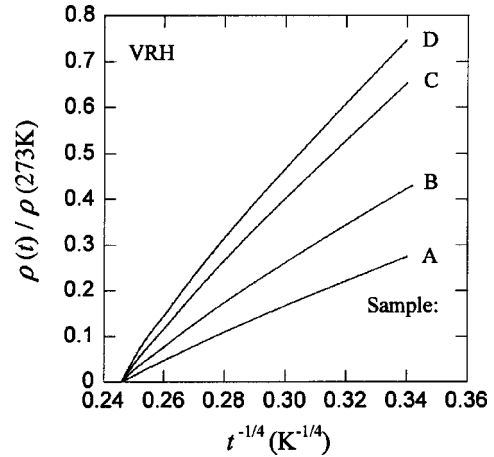| Sample	t_0 (K)	t_1 (K)	t_1^2/t_0 (K)
A	138	317	728
B	139	289	601
C	141	193	264
D	137	119	103

FIG. 7. Logarithm of the normalized resistivity ρ vs temperature t to the power $-1/q$, with $p=4$ according to the VRH model, for samples A–D characterized in Table I. A straight line would indicate the applicability of the VRH model.

the concave curvature shown in Fig. 7, that neither q equal to 1 (NNH) nor 2 (GM) can represent the data.

Figure 8 shows $\rho(t)$ versus $t^{-3/2}$ for samples A–D in the whole measured temperature range. None of the samples exhibit a straight line, i.e., Eq. (7) is also incapable of representing our data.

B. Optical data and analysis

Spectral near-normal reflectance R and transmittance T were measured in the $0.3 < \lambda < 2.5 \ \mu$m wavelength range using a Perkin Elmer Lambda 9 spectrophotometer equipped with an integrating sphere coated with $BaSO_4$. Infrared transmittance was measured at $2.5 < \lambda < 4.5 \ \mu$m and infrared reflectance at $2.5 < \lambda < 30 \ \mu$m using a Perkin Elmer 983 infrared spectrophotometer with an Au mirror as reference. Figures 9(a)–9(e) presents R for $0.3 < \lambda < 30 \ \mu$m and T for $0.3 < \lambda < 2.5 \ \mu$m.
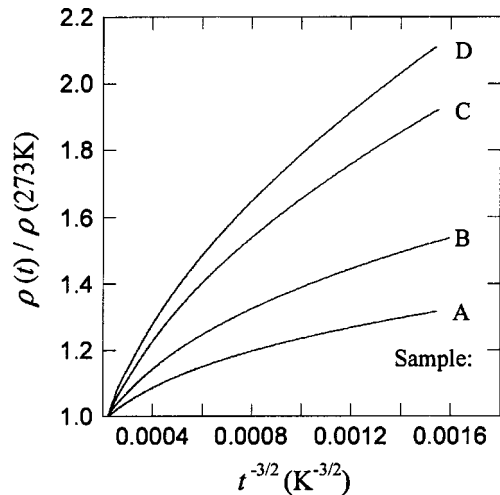

FIG. 8. Normalized resistivity ρ vs temperature t to the power $-3/2$ for samples A–D characterized in Table I. A straight line would indicate the applicability of Eq. (7).
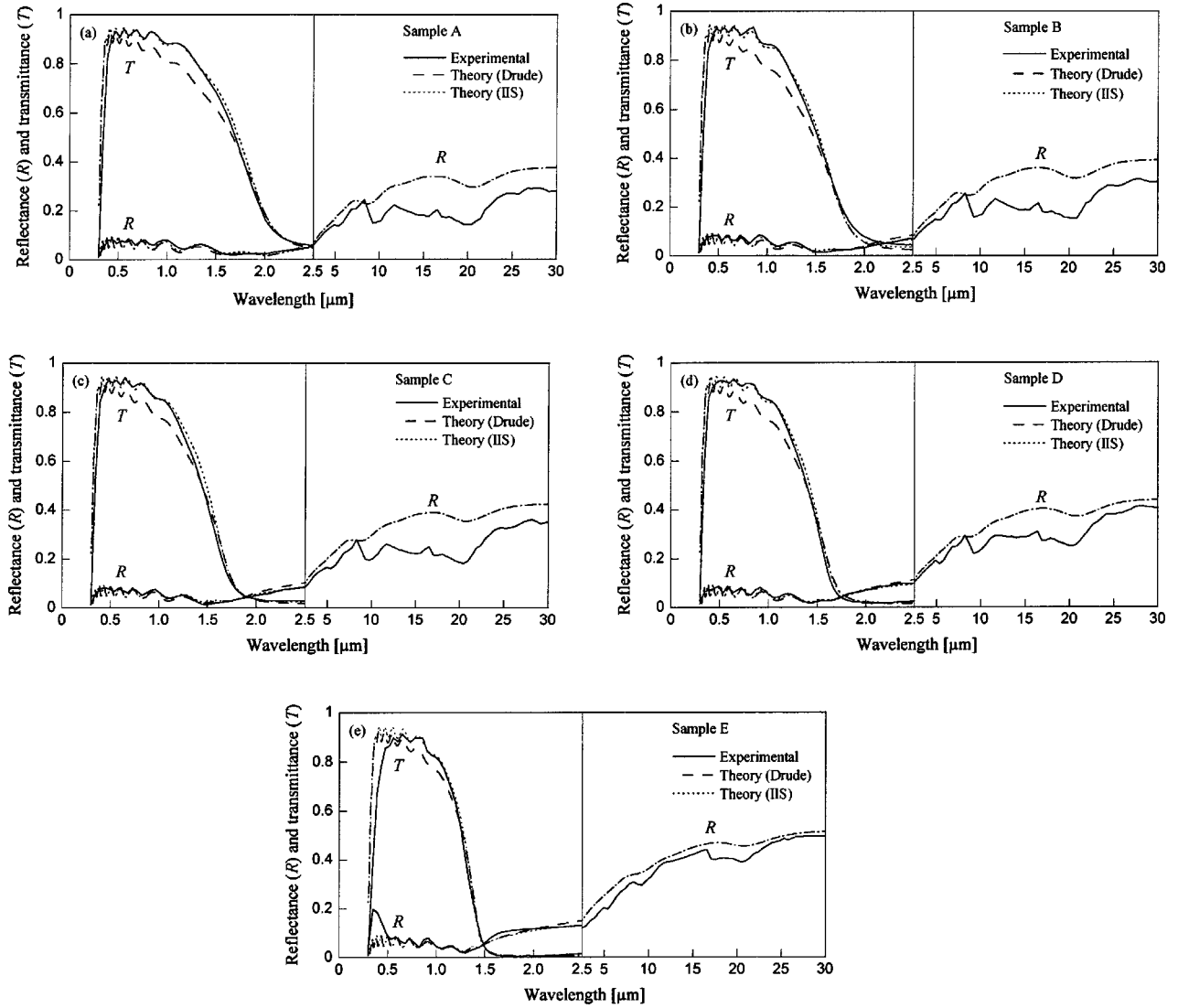
FIG. 9. (a)–(e) Experimental spectral reflectance and transmittance fitted to the Bruggeman effective medium theory including the effect of ionized impurity scattering (IIS). Data are shown for the samples specified in Table I. Note the change in scale at 2.5 μm in wavelength. Theoretical modeling embraces a constant relaxation time (Drude model) and a relaxation time varying as expected for IIS.

The data show that the luminous transmittance exceeds 90% for all samples, except for sample E where this transmittance is slightly lower than 90%. Infrared reflectance data show that R increases upon annealing, with sample E displaying $R \approx 45\%$ at $\lambda = 30 \mu$m.

Figure 10 shows the absorption coefficient α for all samples at $0.3 < \lambda < 2.5 \mu$m as calculated from the method of Hong[25] by the relation

$$\alpha(\lambda) = \frac{1}{\partial} \ln\left(\frac{1 - R(\lambda)}{T(\lambda)} \right), \tag{14}$$

where ∂ is sample thickness. Figure 10 clearly displays an increase in the absorption strength, and a shift of the absorption peak towards shorter wavelengths, upon annealing. These effects are discussed below.

The fitting involves varying the filling factor, starting from the percolation limit. The resistivity of the particles is then given by Eq. (13), by taking ρ to be equal to the mea-

sured dc value. Equation (11) yields a relation between ρ_p, n_e, and τ. Thus we use f and n_e as fitting parameters. Their values determine uniquely the other parameters of the problem, namely ρ_p [by Eq. (13)] and τ_0 [by Eq. (11)]. The mobility is obtained from

$$\mu_p = \frac{e \tau_0}{m_e}. \tag{15}$$

The reflectance and transmittance were calculated for the samples, with proper account taken of the glass substrate. The thin porous ITO film was represented as a single layer,[26] using the dielectric function for the composite film derived from the effective medium theory. The glass substrate was treated in the noncoherent approximation, i.e., only considering light intensities, which were summed up to a total reflectance and transmittance. For the $0.3 < \lambda < 2.5 \mu$m wavelength range we used unpublished optical constants for Corning 7059 glass. Optical constants at $5.0 < \lambda < 30.0 \mu$m
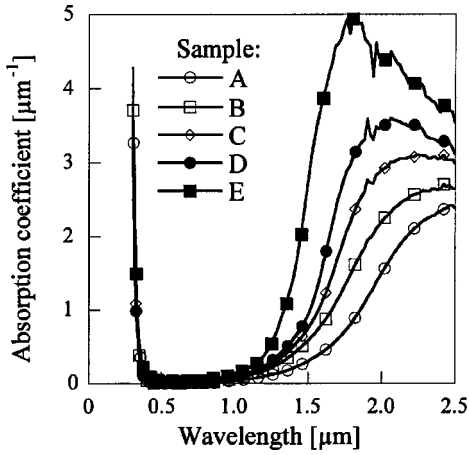
FIG. 10. Spectral absorption coefficient for the samples specified in Table I.

were taken from Ref. 27, and optical constants at $2.0 < \lambda < 5.0 \ \mu$m were calculated from experimental R and T using the method of McPhedran *et al.*[28]

Figures 9(a)–9(e) present data based on the effective medium model fitted to experimental results on R and T. Theoretical descriptions using a constant relaxation time (Drude) as well as a frequency dependent relaxation time (IIS) according to Eq. (12) were employed. Fitting parameters are given in Table III. Both models give identical reflectance in the infrared wavelength range since the frequency dependent relaxation time is introduced at $\omega > \omega_p/\sqrt{\varepsilon_\infty}$. Thus both models gave the same dc-relaxation time.

It is in the visible and near infrared wavelength range that the two models exhibit discrepancies. The difference in R is not significant, due to its low level at visible and near infrared wavelengths in these samples, but differences in T are clearly observed. The Drude model is found to give a lower T than the IIS model. Within the IIS model the relaxation time increases with increasing frequency at $\omega > \omega_p/\sqrt{\varepsilon_\infty}$, and hence the absorption is decreased. This leads to a higher T than the one obtained by the Drude model.

VI. DISCUSSION

A straight line in Fig. 7 would have indicated that the transport property is dominated by a variable range hopping mechanism. However, in the experiments no straight lines

TABLE III. Fits between theory and experiment were made with the shown values of filling factor f, and electron density n_e. Data are given also on the derived mobility μ_p and resistivity ρ_p.

Sample	f	n_e (10^{20} cm^{-3})	μ_p (cm^2/Vs)	ρ_p ($10^{-4} \ \Omega$ cm)
A	0.334	4.0	22.3	7.0
B	0.336	5.0	20.8	6.0
C	0.338	5.5	25.2	4.5
D	0.348	6.0	26.0	4.0
E	0.349	8.0	39.0	2.0

were found. So, a hopping mechanism is not likely. Thus the charge carriers, i.e., the conduction electrons, are not localized and the electrical transport within each ITO particle was found to be due to conduction electrons scattered by ionized impurities. However, the fact that Fig. 8 also does not yield a straight-line behavior clearly shows that the conduction electrons, scattered by ionized impurities, do not govern the temperature dependent electrical dc transport properties in these samples. It is thus evident that the grain boundaries, or the possible insulating barriers between particles or clusters of particles, play a significant role for the transport properties.

A granular-metal charging energy model would not be unexpected, since the samples consist of nanosized ITO particles in a percolating network. However, since $q=4$ gives a clear concave curvature (see Fig. 7), putting $q=2$, as expected in the granular metal model, would then give an even stronger concave curvature, thus indicating that the temperature dependent resistivity is not strongly influenced by the capacitive charging energy of the individual ITO nanoparticles. This gives a clear indication that the particles are sintered into clusters minimizing the charging energy. The good fit between experiment and theory for fluctuation induced tunneling in Fig. 6 gives a strong indication of a film structure consisting of large clusters of particles, and further shows that possible insulating barriers between the individual nanoparticles, within each cluster, do not contribute significantly to the electrical transport properties of the films. For the fluctuation induced tunneling model to be applicable to the experimental data, the charging energy must be negligible compared to the thermal energy $k_B t$, which means that the metallic parts or clusters of sintered ITO particles must be of the order of several μm. Thus the temperature dependent resistivity is dominated by thermally activated voltage fluctuations across the insulating layers, and this mechanism is responsible for the negative TCR.

From Table II it is observed that t_0 is almost identical for all annealing temperatures, and that t_1 decreases with annealing. Equations (4) and (5) yield that the ratio t_1^2/t_0 is proportional to $A V_0^{5/2}$, and from Table II it is clearly shown that this ratio is decreased upon annealing. This means that the barrier height drops with annealing. This is certainly a scenario that is physically reasonable, since the room temperature resistivity also goes down as a result of annealing. Furthermore, as V_0 decreases with annealing the area A of the boundary must increase (assuming a constant width of the barrier) to maintain a constant t_0, which is reasonable since it is likely that sintering occurs due to the annealing, resulting in an increased area between adjacent clusters. From Eqs. (4) and (5) it is obvious that t_0 and t_1, obtained from the fitting, are insufficient for a determination of the three barrier parameters w, A, and V_0. However, an estimation of A and V_0 may be obtained if one assumes a value of w. A reasonable value for the barrier width would be ~ 1 nm, and using the data on t_0 and t_1 for sample D then gives a barrier height of ~ 0.08 eV and an area of ~ 93 nm^2. From the fitting parameters obtained from the fluctuation induced tunneling model for samples A–D the resistivity curves were extrapolated down to low temperatures. It was found that the crossover to a temperature independent resisitivity due to inelastic tunnel-

ing, which should be observable much below t_0,[12] appears at approximately 20 K for all samples.

Sample E, annealed at the highest temperature, exhibits a metallic behavior with a positive TCR in the $130 < t < 300$ K range. Within our framework of interpretation, the conducting clusters have then sintered and formed conducting paths through the whole sample so that a metallic behavior is observed. At $t < 130$ K, the TCR changes sign. Unfortunately we have data only down to 77 K, which makes the analysis of the resistance data below 130 K difficult. However, we can speculate that at low temperatures the resistivity is dominated by ionized impurity scattering, as would be consistent with our optical analysis; see below.

It is clearly seen in Figs. 9(a)–9(e) that the introduction of a frequency dependence in the relaxation time, due to ionized impurity scattering, significantly improves the fit in the visible and near infrared wavelength ranges. This gives a strong indication of a transport mechanism within the ITO nanoparticles that is dominated by ionized impurity scattering. The agreement between theory and experiment is less good further out in the infrared. This may be an effect of grain boundary scattering, which is not included in the models. It is observed that the agreement between theory and experiment improves for samples with larger grain size, i.e., samples E and D.

Furthermore, it is found that all samples display a low filling factor; as seen from Table III, f is close to the percolation limit. This supports the results from our RBS measurements and thickness determinations, which yielded a high degree of porosity. It is also shown that n_e and μ_p increase upon annealing. The ITO nanoparticles in sample E display $n_e \approx 8 \times 10^{20}$ cm^{-3} along with $\mu_p \approx 39$ cm^2/Vs. Room temperature resistivity obtained from the fitting is as low as $\sim 2 \times 10^{-4}$ Ω cm (sample E). This result can be compared to data in the literature and, for example, 7.2×10^{-5} Ω cm was reported for highly transparent thin ITO films prepared by laser evaporation in a magnetic field[29] while a room temperature resistivity of $\sim 1 \times 10^{-4}$ Ω cm is more typically quoted for optimized ITO films.[30,31]

The increase in the mobility is most probably due to two effects: grain growth and improved crystallinity. The lattice may be distorted as a consequence of the introduction of dopant atoms, i.e., Sn^{4+} in the case of ITO. The degree of distortion is represented by the change in the lattice parameter. However, the lattice parameter in our samples is close to the value of undoped In$_2$O$_3$ and, furthermore, no change was observed in the lattice parameter upon annealing. Grain growth results in a decreased number of grain boundaries and, thus, less grain boundary scattering. Our samples display a significant grain growth upon annealing, which may explain the increased mobility.

The increase in n_e may be a result of the increased number of oxygen vacancies upon annealing in a reducing atmosphere at each temperature. Each oxygen vacancy contributes two extra electrons. Since our samples are porous there is a large internal sample surface in contact with the reducing atmosphere. It is therefore possible that oxygen vacancies are created close to the particle surface. However, RBS measurements did not reveal any significant decrease of the oxygen content in the film upon annealing. As a result of the increased n_e, the plasma frequency—responsible for a peak in the absorption—shifts towards shorter wavelengths, which clearly is consistent with the experimental data shown in Fig. 10.

It is obvious from the fitting parameters in Table III that the filling factor of ITO remains low upon annealing. Thus a very important result of our work is that in order to produce samples with low resistivity, an increased filling factor of ITO is required.

VII. CONCLUSIONS

Temperature dependent electrical transport and optical properties in porous thin films comprising ITO nanoparticles with a narrow size distribution have been investigated. In samples annealed at $t \leq 923$ K, the transport properties are dominated by thermally activated voltage fluctuations across insulating barriers as described by a fluctuation induced tunneling model, thus indicating that the sample consists of μm-sized conducting clusters separated by insulating barriers. Samples annealed at 1073 K display a metallic behavior at $t > 150$ K, and the resistivity has a minimum at ~ 130 K.

Effects of annealing on the electrical transport properties within the ITO nanoparticles were investigated by an analysis of optical data using the Bruggeman effective medium theory and accounting for ionized impurity scattering. All samples exhibited a low filling factor of ITO, i.e., a high degree of porosity and a low mass density were obtained. The filling factor remained almost unchanged upon annealing, suggesting that the compaction of the samples was not significant due to the heat treatment. It was found that both the charge carrier concentration and mobility increased upon annealing. The resistivity within the ITO nanoparticles was as low as 2×10^{-4} Ω cm, which is comparable to the resistivity in dense ITO films made by physical vapor deposition. Hence, an efficient densification process is required to obtain films with a low resistivity.

*Present address: Optical Systems Department, Fraunhofer-Institut für Angewandte Optik und Feinmechanik, Schillerstrasse 1, D-07745 Jena, Germany.

†Also at Research Group of Laser Physics of the Hungarian Academy of Sciences, P.O. Box 406, H-6701 Szeged, Hungary.

[1] R. G. Gordon, MRS Bull. **25**, 52 (2000).

[2] Y. Shigesato, S. Takaki, and T. Haranou, Appl. Surf. Sci. **48/49**, 269 (1990).

[3] R. B. H. Tahar, T. Ban, Y. Ohya, and Y. Takahashi, J. Appl. Phys. **83**, 2631 (1997).

[4] N. Kikuchi, E. Kusano, E. Kishio, A. Kinbara, and H. Nanto, J. Vac. Sci. Technol. A **19**, 1636 (2001).

[5] K. Subba Ramaiah, V. Sundara Raja, A. K. Bhatnagar, R. D. Tomlinson, R. D. Pilkington, A. E. Hill, S. J. Chang, Y. K. Su, and F. S. Juang, Semicond. Sci. Technol. **15**, 676 (2000).

[6] C. G. Granqvist and A. Hultåker, Thin Solid Films **411**, 1 (2002).

[7] I. Hamberg, C. G. Granqvist, K. F. Berggren, B. Sernelius, and L. Engström, Phys. Rev. B **30**, 3240 (1984).

[8] M. Toki and M. Aizawa, J. Sol-Gel Sci. Technol. **8**, 717 (1997).

[9] N. Nadaud, M. Nanot, and P. Boch, J. Am. Ceram. Soc. **77**, 843 (1994).

[10] T. Kayukawa, H. Shigetani, and M. Senna, J. Mater. Sci. Lett. **14**, 252 (1995).

[11] J. Ederth, A. Hultåker, P. Heszler, G. A. Niklasson, C. G. Granqvist, A. R. van Doorn, C. van Haag, M. J. Jongerius, and D. Burgard, Proc. Soc. Photo-Opt. Instrum. Eng. **4590**, 280 (2001).

[12] P. Sheng, Phys. Rev. B **21**, 2180 (1980).

[13] D. A. G. Bruggeman, Ann. Phys. (Leipzig) **24**, 636 (1935).

[14] A. Hultåker, A. Hoel, C. G. Granqvist, A. van Doorn, M. J. Jongerius, and D. Burgard, in *Nanophase and Nanocomposite Materials IV*, edited by S. Komarneni, J. C. Parker, R. A. Vaia, G. Q. Lu, and J. Matsuchita, MRS Symposia Proceedings No. 703 (Materials Research Society, Pittsburgh, 2002), p. 185.

[15] B. D. Cullity, *Elements of X-Ray Diffraction* (Addison-Wesley, Reading, MA, 1956).

[16] N. Mott, *Metal-Insulator Transitions* (Taylor and Francis, London, 1990).

[17] Z. H. Wang, M. S. Dresselhaus, G. Dresselhaus, K. A. Wang, and P. C. Eklund, Phys. Rev. B **49**, 15 890 (1994).

[18] B. R. Nag, *Electron Transport in Compound Semiconductors* (Springer, Berlin, 1980), Vol. 11.

[19] J. Ederth, G. A. Niklasson, A. Hultåker, P. Heszler, C. G. Granqvist, A. van Doorn, M. J. Jongerius, and D. Burgard, J. Appl. Phys. **93**, 984 (2003).

[20] I. Hamberg, Ph.D. thesis, Chalmers University of Technology, Gothenburg, Sweden, 1984.

[21] I. Hamberg and C. G. Granqvist, J. Appl. Phys. **60**, R123 (1986).

[22] C. G. Granqvist and O. Hunderi, Phys. Rev. B **18**, 1554 (1978).

[23] Y. Suzuki, F. Niino, and K. Katoh, Thin Solid Films **218**, 30 (1997).

[24] K. Utsumi, O. Matsunaga, and T. Takahata, Thin Solid Films **334**, 30 (1998).

[25] W. Q. Hong, J. Phys. D **22**, 1384 (1989).

[26] Z. Knittl, *Optics of Thin Films* (Wiley, New York, 1976).

[27] G. Ljungdahl, Ph.D. thesis, Uppsala University, Uppsala, Sweden, 1992.

[28] R. C. McPhedran, L. C. Botten, D. R. McKenzie, and R. P. Netterfield, Appl. Opt. **23**, 1197 (1984).

[29] A. Suzuki, T. Matsushita, T. Aoki, Y. Yoneyama, and M. Okuda, Jpn. J. Appl. Phys. **40**, L401 (2001).

[30] Y. Suzuki, F. Niino, and K. Katoh, Thin Solid Films **218**, 30 (1997).

[31] K. Utsumi, O. Matsunaga, and T. Takahata, Thin Solid Films **334**, 30 (1998).